

Northumbria Research Link

Citation: Yang, Wooseok, Kim, Jin Hyun, Hutter, Oliver, Phillips, Laurie J., Tan, Jeiwan, Park, Jaemin, Lee, Hyungsoo, Major, Jonathan D., Lee, Jae Sung and Moon, Jooho (2020) Benchmark performance of low-cost Sb₂Se₃ photocathodes for unassisted solar overall water splitting. Nature Communications, 11 (1). p. 861. ISSN 2041-1723

Published by: Nature Publishing

URL: <https://doi.org/10.1038/s41467-020-14704-3> <<https://doi.org/10.1038/s41467-020-14704-3>>

This version was downloaded from Northumbria Research Link:
<http://nrl.northumbria.ac.uk/id/eprint/42214/>

Northumbria University has developed Northumbria Research Link (NRL) to enable users to access the University's research output. Copyright © and moral rights for items on NRL are retained by the individual author(s) and/or other copyright owners. Single copies of full items can be reproduced, displayed or performed, and given to third parties in any format or medium for personal research or study, educational, or not-for-profit purposes without prior permission or charge, provided the authors, title and full bibliographic details are given, as well as a hyperlink and/or URL to the original metadata page. The content must not be changed in any way. Full items must not be sold commercially in any format or medium without formal permission of the copyright holder. The full policy is available online: <http://nrl.northumbria.ac.uk/policies.html>

This document may differ from the final, published version of the research and has been made available online in accordance with publisher policies. To read and/or cite from the published version of the research, please visit the publisher's website (a subscription may be required.)

ARTICLE


<https://doi.org/10.1038/s41467-020-14704-3>

OPEN

Benchmark performance of low-cost Sb_2Se_3 photocathodes for unassisted solar overall water splitting

Wooseok Yang ^{1,4}, Jin Hyun Kim^{2,4}, Oliver S. Hutter ³, Laurie J. Phillips ³, Jeiwan Tan¹, Jaemin Park¹, Hyungsoo Lee¹, Jonathan D. Major^{3✉}, Jae Sung Lee^{2✉} & Jooho Moon ^{1✉}

Determining cost-effective semiconductors exhibiting desirable properties for commercial photoelectrochemical water splitting remains a challenge. Herein, we report a Sb_2Se_3 semiconductor that satisfies most requirements for an ideal high-performance photoelectrode, including a small band gap and favourable cost, optoelectronic properties, processability, and photocorrosion stability. Strong anisotropy, a major issue for Sb_2Se_3 , is resolved by suppressing growth kinetics via close space sublimation to obtain high-quality compact thin films with favourable crystallographic orientation. The Sb_2Se_3 photocathode exhibits a high photocurrent density of almost 30 mA cm^{-2} at 0 V against the reversible hydrogen electrode, the highest value so far. We demonstrate unassisted solar overall water splitting by combining the optimised Sb_2Se_3 photocathode with a BiVO_4 photoanode, achieving a solar-to-hydrogen efficiency of 1.5% with stability over 10 h under simulated 1 sun conditions employing a broad range of solar fluxes. Low-cost Sb_2Se_3 can thus be an attractive breakthrough material for commercial solar fuel production.

¹Department of Materials Science and Engineering, Yonsei University, 50 Yonsei-ro, Seodaemun-gu, Seoul 03722, Republic of Korea. ²School of Energy and Chemical Engineering, Ulsan National Institute of Science and Technology, Ulsan 44919, South Korea. ³Stephenson Institute for Renewable Energy, Physics Department, University of Liverpool, Liverpool L69 7XF, UK. ⁴These authors contributed equally: Wooseok Yang, Jin Hyun Kim. ✉email: Jon.Major@liverpool.ac.uk; jlee1234@unist.ac.kr; jmoon@yonsei.ac.kr

Molecular hydrogen production via photoelectrochemical (PEC) splitting of water is a promising solution toward a zero-carbon-based society. In order to produce sustainable H_2 for a scale commensurate with the global energy demand, high efficiency and low cost, both of which highly depend on the semiconductor materials used in the PEC system, should be achieved. As the solar-to-hydrogen (STH) efficiency of PEC devices using expensive photovoltaic-grade III–V semiconductors has approached the theoretical maximum¹, the research community is now recognising the importance of exploring low-cost materials exhibiting good optoelectronic properties². With this consideration, nearly all recent critical evaluations^{3–5} pertaining to artificial photosynthesis have urged the development of new light absorbers. According to theoretical calculations^{6,7}, two different light absorbers—having a band gap (E_g) of ~ 1.8 eV for the top electrodes and 1.0–1.3 eV for the bottom electrodes—are required for realising STH efficiencies of $>23\%$ in the D4 (dual light absorber: four photons to one H_2) tandem cell. Further requirements for suitable semiconductors for PEC water splitting include a large light absorption coefficient (α), high mobility, easy processability without secondary phases, and stability to photocorrosion. In this regard, most emerging cost-competitive photoelectrode materials for PEC water splitting, such as TiO_2 ($E_g \sim 3.2$ eV)⁸, Fe_2O_3 ($E_g \sim 2.2$ eV)⁹, $BiVO_4$ ($E_g \sim 2.4$ eV)¹⁰, and Cu_2O ($E_g \sim 2.0$ eV)¹¹, are deemed unsuitable for the bottom photoelectrode due to their large E_g . Although the E_g of $Cu_2ZnSn(S,Se)_4$ semiconductor, which is another earth-abundant material applicable for PEC water splitting, varies from 1.0 to 1.5 eV depending on the composition, the pure-phase compound suffers from severe difficulty of synthesis due to the narrow stoichiometric window¹². It is worth mentioning that the secondary phase issue, i.e. the formation of undesirable detrimental phases during processing, could pose a major obstacle to large-scale commercialisation. In recent years, various low-cost semiconductors have emerged, such as Cu_2S ($E_g \sim 1.5$ eV)¹³, $CuFeO_2$ ($E_g \sim 1.5$ eV)¹⁴, $CuBi_2O_4$ ($E_g \sim 1.7$ eV)¹⁵, $CuSbS_2$ ($E_g \sim 1.5$ eV)¹⁶, and SnS ($E_g \sim 1.3$ eV)¹⁷. However, none of them have satisfied all the requirements for an ideal semiconductor for PEC water splitting. Therefore, a breakthrough material for realising practical STH conversion is urgently required⁴.

Sb_2Se_3 offers many advantageous properties that make it a nearly ideal semiconductor material for PEC water splitting. First, it has a small E_g of 1.1–1.2 eV. In addition, it is a low-cost semiconductor (the cost of Sb is similar to that of Cu)¹⁸ and exhibits attractive optoelectronic properties ($\alpha > 10^5$ cm⁻¹ and high mobility of ~ 10 cm² V⁻¹ s⁻¹)^{19,20}. Moreover, the thermodynamic properties of the Sb–Se system allow only stable orthorhombic Sb_2Se_3 phases without any secondary phases²¹, avoiding severe secondary phase issues commonly observed in other multivalent compound materials. It has also been reported that Sb_2Se_3 is intrinsically stable towards photocorrosion in strong acidic media unlike Cu_2O , which is vulnerable to photocorrosion²². Owing to these merits, the photocurrent density of the Sb_2Se_3 photocathode has improved rapidly from the initially reported value of 2.5 mA cm⁻² to 17.5 mA cm⁻² at 0 V against the reversible hydrogen electrode (RHE) over the short period of its development^{23–26}. However, it is still far below the theoretical maximum (about 40 mA cm⁻², assuming a 1.2 eV E_g and a 100% incident photon-to-current efficiency (IPCE)). In addition, it has been reported that the onset potential of Sb_2Se_3 photocathodes can be enhanced up to 0.47 V_{RHE}²⁷, but the photovoltage and fill factor should be further improved to realise unassisted water splitting.

As Sb_2Se_3 has a one-dimensional (1D) crystal structure, it tends to grow with the morphology of 1D nanostructures, which makes

synthesis of compact Sb_2Se_3 thin films difficult²⁸. In the case wherein a light-absorbing material has a low absorption coefficient and poor electrical properties (e.g. short carrier diffusion length), 1D nanostructuring could be an attractive strategy for enhancing the performance. However, in the previously reported Sb_2Se_3 photocathodes, probably owing to its good optoelectronic properties, planar-type Sb_2Se_3 exhibited better performance compared with that of its elongated 1D structured counterpart^{24,27}. One possible reason is that the incomplete coverage of Sb_2Se_3 films, due to the complicated 1D morphology, can result in direct contact between the substrate and an n-type layer, which acts as a recombination centre. In addition, because the carrier transport in Sb_2Se_3 along the [001] direction is more efficient than that along the [010] and [100] directions owing to its anisotropic crystallographic nature²⁰, the p–n junction should be formed along the [001] direction to maximise the separation of the photo-generated charges. In the 1D Sb_2Se_3 system, however, the p–n junction generally is formed along the [010] or [100] directions, resulting in inefficient charge separation. Thus compact film-type Sb_2Se_3 with favourable crystallographic orientation for efficient charge separation (i.e. vertically aligned $(Sb_4Se_6)_n$ nanoribbons) should be obtained to achieve high-performance Sb_2Se_3 photocathodes. However, as molecular inks for Sb_2Se_3 already contain 1D $[Sb_4Se_7]^{2-}$ chains in the solution^{24,27}, it is a daunting task to obtain compact thin Sb_2Se_3 films via solution processing.

Here we report high-quality dense Sb_2Se_3 thin films obtained by the close space sublimation (CSS) method, which is known to be a low-cost, large-area, high-yield deposition technique for preparing light-absorbing semiconductors, such as cadmium telluride²⁹ and $CH_3NH_3PbI_3$ ³⁰. We implement a fast cooling strategy as well as the two-step CSS method³¹, enabling pin-hole-free and smooth Sb_2Se_3 thin films with well-oriented $(Sb_4Se_6)_n$ ribbons. The resulting Sb_2Se_3 thin-film-based photocathodes reveal a highest photocurrent density close to 30 mA cm⁻² at 0 V_{RHE}. The performance of the newly developed Sb_2Se_3 photocathode is utilised by unassisted overall water splitting PEC cells after judiciously optimising the photovoltage and electrolyte compatibility to the $BiVO_4$ photoanode. The D4 tandem cell of Sb_2Se_3 – $BiVO_4$ in a neutral phosphate buffer successfully demonstrates an impressive STH efficiency of 1.5% with 10 h of stability. Realisation of the Sb_2Se_3 -based tandem device, capable of harvesting a broad range of photons with the readily obtained earth-abundant semiconductor, allows us to envision practical solar hydrogen production via efficient and cost-competitive PEC water splitting.

Results

Fabrication of compact and well-oriented Sb_2Se_3 thin films. In order to avoid the formation of the thermodynamically favourable 1D structure as well as induce the metastable thin film morphology of Sb_2Se_3 , we tried to kinetically suppress the rearrangement of $(Sb_4Se_6)_n$ nanoribbons by employing a two-step deposition where a low-temperature (340 °C) seed layer was deposited prior to the high-temperature (460 °C) deposition³¹. In general, the CSS system employs one-step deposition at a high temperature (e.g. 400–550 °C for CdTe) to achieve a suitable growth rate²⁹. Owing to the highly anisotropic nature of Sb_2Se_3 , however, the low-temperature deposition is an imperative step to obtain a compact morphology. At the first deposition step of 340 °C, a compact thin film could be obtained, whereas an elongated 1D structure with incomplete coverage was observed when a temperature of 460 °C was applied directly (Supplementary Fig. 1). Figure 1a–c show the microstructures of Sb_2Se_3 thin films deposited on an Au/fluorine-doped tin oxide (FTO) substrate by the two-step CSS deposition process (i.e. successive depositions at 340 and 460 °C followed by cooling the chamber

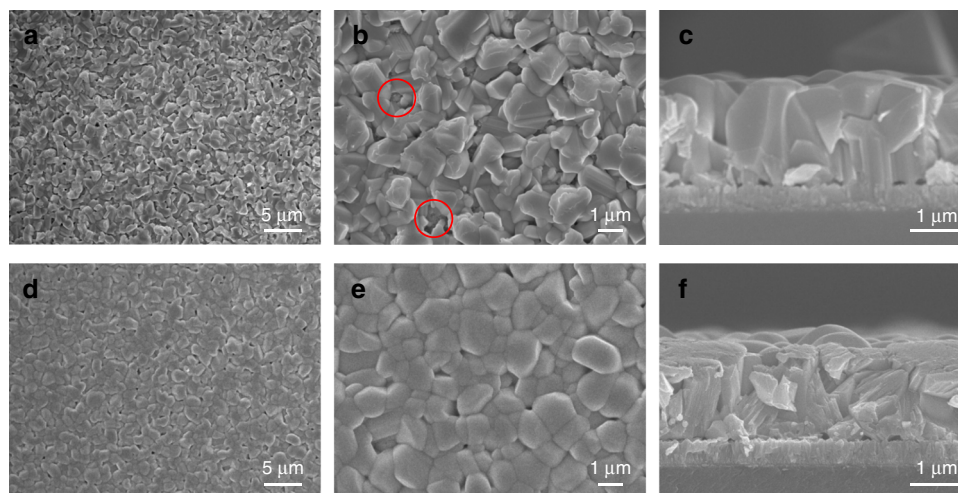


Fig. 1 Microstructures and crystallographic orientation of Sb_2Se_3 thin films. **a–f** SEM images of **a–c** slow-cooling Sb_2Se_3 and **d–f** fast-cooling Sb_2Se_3 .

naturally after deposition). The role of the Au layer in Sb_2Se_3 photoelectrodes, which facilitates the transfer of photo-generated holes, has been discussed in previous reports on Sb_2Se_3 for PEC water splitting^{26,32} and thin-film solar cells³³. Despite the film-type morphology, there were some pin-holes resulting in exposure of the substrate (red circles in Fig. 1b) with the faceted morphology of the Sb_2Se_3 thin films. Interestingly, it was found that a much smoother pin-hole-free surface was achieved when N_2 gas was passed during the cooling process after deposition under the same conditions (i.e. successive depositions at 350 and 450 °C), as shown in Fig. 1d–f. We denoted the sample prepared with N_2 -assisted cooling as the ‘fast-cooling’ sample, while the naturally cooled sample was denoted as the ‘slow-cooling’ sample. The cooling rates for the fast cooling and the slow cooling until it has reached 200 °C are approximately 15.7 and 11.3 °C min^{−1}, respectively. The detailed differences between the two samples, including grain size distribution and crystallographic orientations, are shown in Supplementary Figs. 2–4.

On comparing the morphological and crystallographic differences between the fast- and slow-cooling samples, it was obvious that the N_2 flow during the cooling process significantly affects the morphology and crystallographic orientation. As mentioned above, because Sb_2Se_3 has a strong 1D anisotropic nature, thermodynamically favourable sharp and facet morphologies are inevitably obtained when kinetically sufficient time is provided (i.e. slow cooling). In contrast, in case of fast cooling, which offers insufficient time to reach the thermodynamically stable morphology, a metastable smooth morphology can be achieved. This explanation is supported by the solution-processed Sb_2Se_3 , in which 1D nanostructures were observed when sufficient Se precursor was provided, while the metastable planar-type Sb_2Se_3 was obtained in Se-deficient conditions²⁷. In addition, a slight change in X-ray diffraction (XRD) data implied that the ribbons likely move during the cooling process, presumably due to the low melting temperature of Sb_2Se_3 (~608 °C). Thus it can be reasonably concluded that, in order to fabricate compact thin-film-type Sb_2Se_3 with favourably oriented $(\text{Sb}_4\text{Se}_6)_n$ ribbons, rearrangement of the ribbons should be kinetically suppressed as much as possible to prevent the formation of thermodynamically stable 1D structures. Obtained with kinetically controlled growth, it was possible to obtain Sb_2Se_3 thin films with a compact structure as well as well-oriented ribbons, both of which are expected to be favourable for better performance.

PEC performance of CSS- Sb_2Se_3 photocathodes. Figure 2a, b show the PEC performance of $\text{RuO}_x/\text{TiO}_2/\text{Sb}_2\text{Se}_3/\text{Au}/\text{FTO}$ photocathodes using fast- and slow-cooling Sb_2Se_3 films measured in pH 1 electrolytes. As we mentioned above, the Au layer acts as a hole-selective contact, which facilitates the transfer of photo-generated holes while blocking the electrons backflow^{32,33}. Without the Au layer, Sb_2Se_3 photocathodes revealed relatively poor performance while nearly similar morphology of Sb_2Se_3 was observed (Supplementary Fig. 5), which verifies the role of the Au layer not affecting the growth of Sb_2Se_3 but assisting the transfer of photo-generated charges. The RuO_x catalytic layer was deposited by the PEC method, while atomic layer deposition (ALD) was used for the TiO_2 layer, similar to a previous study³². In both samples, the onset potentials shifted towards a positive direction after the first scan due to activation of the RuO_x catalyst³⁴. The photocurrent density of the fast-cooling sample approached 30 mA cm^{−2} at 0 V_{RHE}, which is not only the highest value obtained for a Sb_2Se_3 photocathode but also among the best observed for all photoelectrodes used in PEC water splitting so far. Note that the data shown in Fig. 2 were obtained from the best-performing device, while normally 25–30 cm^{−2} at 0 V_{RHE} photocurrent density was observed in the fast-cooling Sb_2Se_3 -based photocathodes. The previously reported photocurrent densities of photoelectrodes for PEC water splitting are shown in Supplementary Fig. 6. Given the low-cost and relatively short history of Sb_2Se_3 as well as the simple preparation and low material usage due to the high α , the high photocurrent density of ~30 mA cm^{−2} at 0 V_{RHE} clearly demonstrates the strong potential of Sb_2Se_3 as a promising photocathode material.

While the fast-cooling sample revealed a record photocurrent density, the photocurrent density of the slow-cooling sample with a RuO_x co-catalyst, which had a facet morphology, was relatively low (~17 mA cm^{−2} at 0 V_{RHE}, Fig. 2b). Figure 2c exhibits the half-cell STH conversion efficiencies (HC-STH) calculated from the third scans in Fig. 2a, b according to the equation $\text{HC-STH} = I_{\text{ph}} \times (E_{\text{RHE}} - E_{\text{H}^+/\text{H}_2}) / P_{\text{SUN}} \times 100\%$, where I_{ph} is the photocurrent density obtained under an applied bias of E_{RHE} , $E_{\text{H}^+/\text{H}_2}$ is 0 V_{RHE}, and P_{SUN} is 100 mW cm^{−2}. It is worth noting that the maximum value of HC-STH in the fast cooling was observed at a more positive potential of 0.16 V_{RHE} compared with that of the slow-cooling counterpart (0.09 V_{RHE}), indicating that the fast-cooling strategy is advantageous for not only the photocurrent but also the photovoltage and fill factor. As shown in Fig. 2d, both fast- and

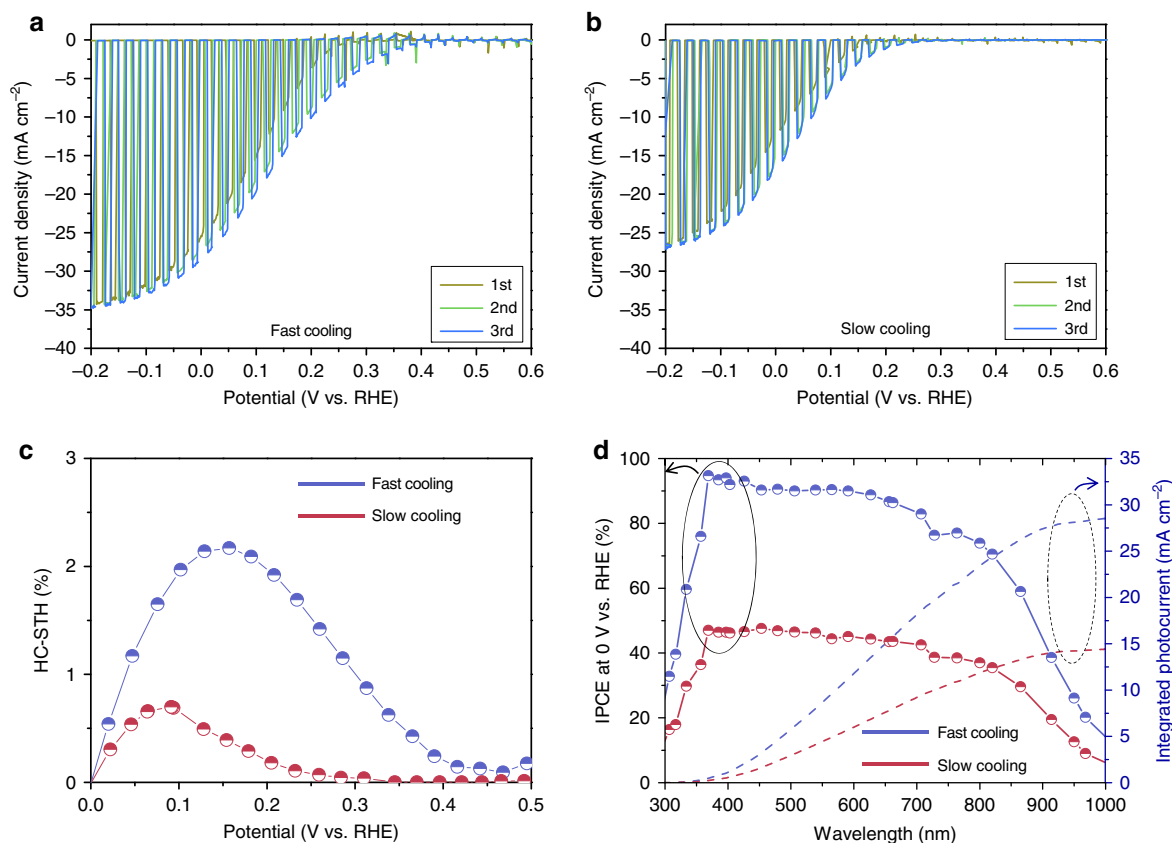


Fig. 2 PEC performance of $\text{RuO}_x/\text{TiO}_2/\text{Sb}_2\text{Se}_3/\text{Au}/\text{FTO}$ photocathodes in pH 1 H_2SO_4 electrolyte. **a**, **b** J - V curves of **a** fast- and **b** slow-cooling samples under simulated 1 sun air mass 1.5 G chopped illumination at a scan speed of 5 mV s^{-1} from positive to negative potential and **c** corresponding HC-STH efficiencies. **d** Wavelength-dependent IPCE and integrated photocurrent density of fast- and slow-cooling samples measured at 0 V_{RHE} . Source data used to generate this figure can be found in the Source Data file.

slow-cooling Sb_2Se_3 photocathodes were able to harvest photons over 1000 nm, but the IPEC was much higher for the fast-cooling sample over the entire wavelength. Because the optical properties (e.g. surface reflection of $\text{Sb}_2\text{Se}_3/\text{Au}/\text{FTO}$ samples) for the fast- and slow-cooling samples were nearly identical (Supplementary Fig. 7), optical properties can be excluded from the potential origin of the difference noted in the performance. In addition, a similar performance was observed when a Pt co-catalyst was used ($\text{Pt}/\text{TiO}_2/\text{Sb}_2\text{Se}_3/\text{Au}/\text{FTO}$, Supplementary Fig. 8): thus we can conclude that the performance difference arose not from the co-catalyst but presumably from the $\text{TiO}_2/\text{Sb}_2\text{Se}_3$ junction.

In order to understand the performance difference observed for the fast- and slow-cooling samples, we performed Kelvin probe force microscopy (KPFM) analyses, which allowed us to investigate the topography and surface potential distribution. Figure 3a, c and b, d show the surface topography and surface potential of $\text{TiO}_2/\text{Sb}_2\text{Se}_3$ devices, respectively. The fast-cooling $\text{TiO}_2/\text{Sb}_2\text{Se}_3$ revealed relatively uniform distribution of surface topography and potential, as shown in Fig. 3a, b. On the other hand, some noticeable high-potential regions, as represented by the bright yellow colour in Fig. 3d, were observed for the slow-cooling $\text{TiO}_2/\text{Sb}_2\text{Se}_3$ sample. Topography and potential line profiling for the fast-cooling sample suggested that the potential resembles the topography of $\text{TiO}_2/\text{Sb}_2\text{Se}_3$ (Fig. 3e), indicating a lower surface potential at the grain boundaries of Sb_2Se_3 ³⁵. In the fast-cooling sample, the separation of the photo-generated electrons and holes efficiently occurred along the vertically aligned $[\text{Sb}_4\text{Se}_6]_n$ ribbons, as shown in Fig. 3g, owing to the p-n junction and relatively small lateral potential difference. In contrast, in the slow-cooling sample, the surface potential increased significantly with a rapid drop in the topography (Fig. 3f),

indicating direct contact between the n-type TiO_2 layer and substrate due to pin-holes. It might be worth to note that the height recorded by AFM and KPFM ranged from a few nm to hundreds nm and even sometimes μm scale^{36,37}. In such a case, the photo-excited electrons can be extracted laterally to the ribbons and they can recombine with the holes at the back contact as shown in Fig. 3h due to the large electric field across the p-n junction. It is widely known that direct contact between the top and bottom contact (i.e., in this case, the TiO_2 and Au layers) can cause significant degradation of the performance, even in the case of the chemical composition and optoelectronic properties have negligible differences. For example, Luo et al. reported the effect of a thin blocking layer to prevent shunt pathways, thereby enabling much higher performance in Cu_2O nanowire photocathodes without any noticeable differences in chemical composition and morphology³⁸. The KPFM results clearly demonstrated the importance of pin-hole-free compact thin films in preventing the recombination and the performance degradation mechanism in the presence of pin-holes, which had not yet been experimentally demonstrated.

Sb_2Se_3 photocathodes in unassisted water splitting. Despite the high photocurrent density of the fast-cooling CSS- Sb_2Se_3 photocathodes, there remain some issues prior to achieving unassisted water splitting by fabricating a tandem device in conjunction with the photoanode. After the optimisation of the electrolyte and the onset potential (Supplementary Figs. 9–11), we decided to use a Pt co-catalyst for the PEC tandem device. With the Pt co-catalyst, we inserted a CdS layer between TiO_2 and the fast-cooling Sb_2Se_3 to further enhance the onset potential, as shown in Fig. 4a²⁷. The

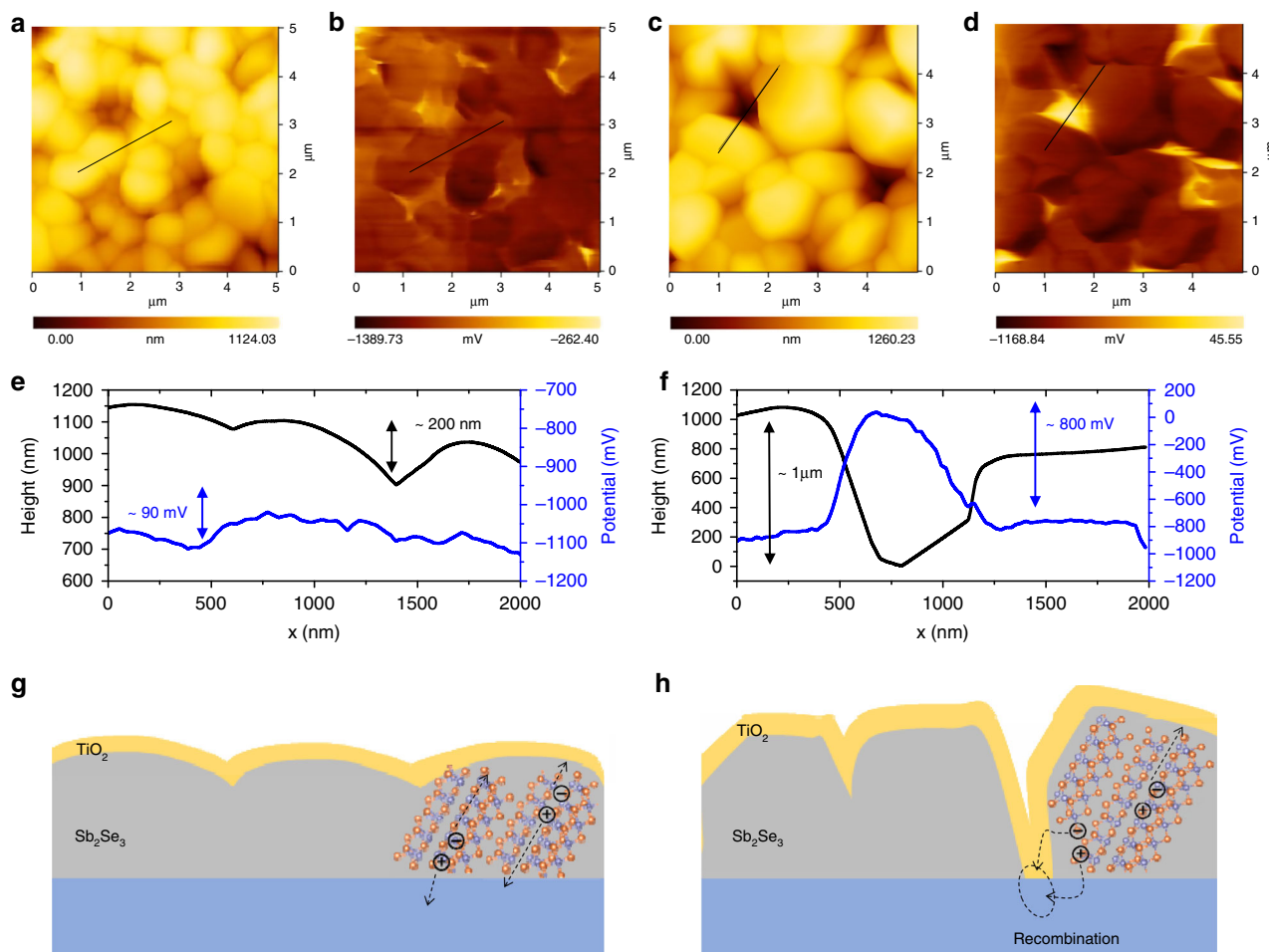


Fig. 3 Topography and surface potential of $\text{TiO}_2/\text{Sb}_2\text{Se}_3$ according to KPFM analysis. **a, c** Topography of **a** fast- and **c** slow-cooling samples. **b, d** Surface potential of **b** fast- and **d** slow-cooling samples. **e, f** Topography and potential line profile (obtained from scanning the black lines in Fig. 3a-d) for **e** fast- and **f** slow-cooling samples. **g, h** Schematics showing possible charge separation and recombination in **g** fast- and **h** slow-cooling samples. Source data used to generate this figure can be found in the Source Data file.

thickness of the CdS and TiO_2 layers were approximately 50 and 30 nm, respectively (Supplementary Fig. 12). Upon deposition of the CdS layer, the onset potential of the Sb_2Se_3 photocathode shifted up to $0.5 V_{\text{RHE}}$ and the fill factor was also significantly enhanced (Fig. 4b). As a result, the maximum HC-STH increased from 2.33% to 3.4%, and the potential at which the maximum HC-STH was observed also shifted from 0.18 to $0.26 V_{\text{RHE}}$, as shown in Fig. 4c. Therefore, despite the slightly decreased photocurrent density at $0 V_{\text{RHE}}$, $\text{Pt}/\text{TiO}_2/\text{CdS}/\text{Sb}_2\text{Se}_3$ configuration was more suitable for the PEC tandem device. The enhanced onset potential and fill factor could be attributed to the reduced band mismatch between TiO_2 and Sb_2Se_3 ²⁷. Figure 4d shows the IPCE spectra for Sb_2Se_3 photocathodes with and without CdS layers, suggesting that the IPEC of 300–500 nm decreased with the thickness of the CdS layer. The reduced IPCE values imply that the photons absorbed by the CdS ($E_g \sim 2.4 \text{ eV}$, $\sim 516.6 \text{ nm}$) were unable to contribute to the photocurrent density. Therefore, when the thickness of the CdS layer increased, the photocurrent density decreased, whereas the onset potential remained the same (i.e. $\sim 0.5 V_{\text{RHE}}$), indicating the necessity of careful optimisation of the CdS layer thickness (Supplementary Fig. 13).

D4 tandem cell for unbiased solar overall water splitting. Since the band gap of Sb_2Se_3 is 1.2 eV, which is suitable for realising a D4 tandem cell as a bottom electrode with a different top light

absorber³⁹, we fabricated tandem cells coupled with BiVO_4 -based photoanodes ($E_g \sim 2.4 \text{ eV}$), which have been widely used for high-performance photocathode-photoanode tandem cells¹⁰ (Fig. 5a). The $\text{H}_2\text{Mo}:\text{BiVO}_4$ photoanode used here revealed good transparency (Supplementary Fig. 14) and performance ($\sim 4.7 \text{ mA cm}^{-2}$ at $1.23 V_{\text{RHE}}$ and onset potential of $0.25\text{--}0.3 V_{\text{RHE}}$) as a top light absorber. To achieve high efficiency, further optimisation of the electrolyte was conducted for the tandem cell comprising two photoelectrodes involving opposite reactions (Supplementary Figs. 15–18).

As shown in Fig. 5b, the operating point of the two photoelectrodes, as estimated by the intersection of two J - V curves, was approximately 1.2 mA cm^{-2} at $0.4 V_{\text{RHE}}$, which corresponded to a STH efficiency of 1.5%. It should be noted that photocurrent density of BiVO_4 at $0.4 V_{\text{RHE}}$ varies from 1.2 to 0.8 mA cm^{-2} , thus the overall STH efficiencies of the tandem cell range from 1.48% to 0.98%. In addition, the polarisation curves of BiVO_4 -Pt (as the counter electrode) and BiVO_4 - Sb_2Se_3 (as the counter electrode) demonstrated a $\sim 0.5 \text{ V}$ anodic shift induced by the Sb_2Se_3 photocathode, indicating that the Sb_2Se_3 photocathode provided a photovoltage of 0.5 V (Fig. 5c). The BiVO_4 - Sb_2Se_3 tandem cell exhibited 1.2 mA cm^{-2} at 0 V against the counter electrode (i.e. unbiased conditions), which was in agreement with the estimated value according to the overlapped J - V curves shown in Fig. 5b. This observation verified that the total photovoltage of 1.45 V (0.52 V from the Sb_2Se_3 photocathode

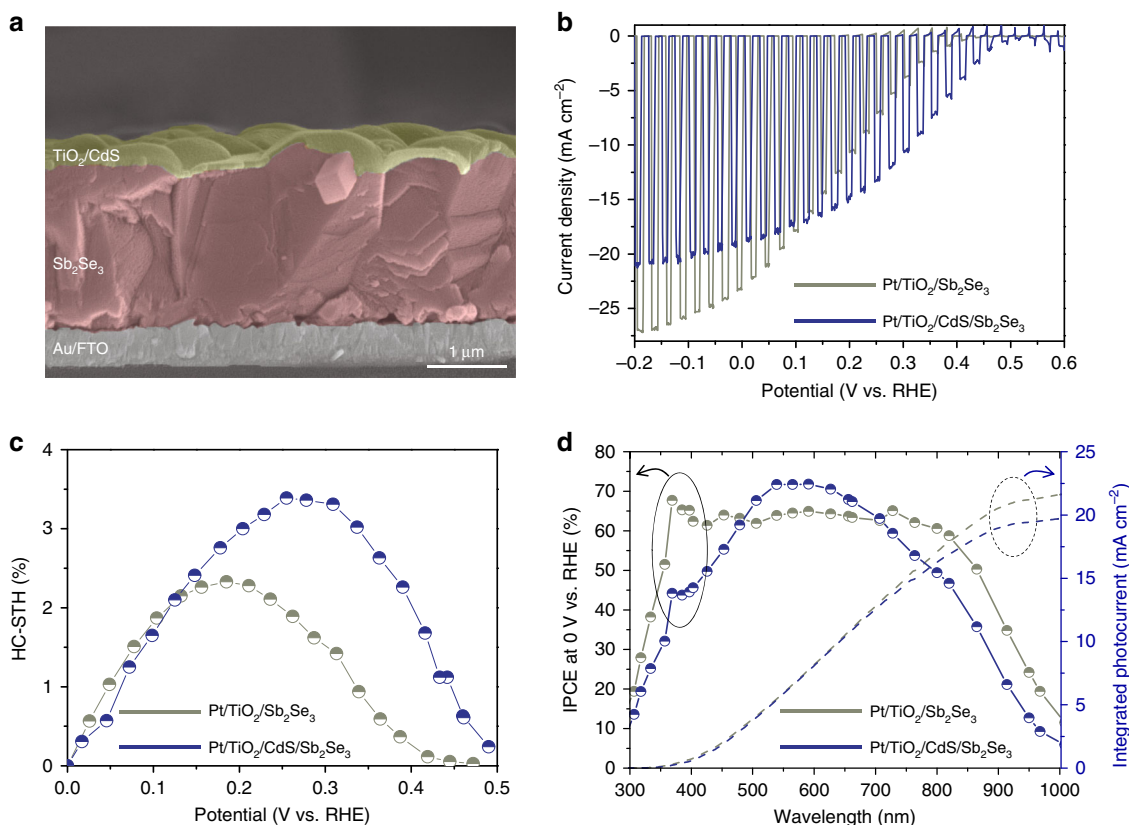


Fig. 4 Microstructure and PEC performance of Pt/TiO₂/CdS/Sb₂Se₃/Au/FTO photocathodes. **a** Cross-sectional SEM image of TiO₂/CdS/Sb₂Se₃ on Au/FTO substrate. **b** *J*-*V* curves for Sb₂Se₃ photocathodes with/without a CdS layer in pH 1 H₂SO₄ under simulated 1 sun air mass 1.5 G chopped illumination at a scan speed of 5 mV s⁻¹ from positive to negative potential and **c** corresponding HC-STH efficiencies. **d** Wavelength-dependent IPCE at 0 V_{RHE} of Sb₂Se₃ photocathodes with/without CdS layer. Source data used to generate this figure can be found in the Source Data file.

and 0.93 V from the BiVO₄ photoanode) was sufficient to implement unbiased overall water splitting, resulting in evolution of both H₂ and O₂, by overcoming the thermodynamic potential requirement (1.23 V). In comparison to previously reported photoelectrodes, the total photovoltage of 1.45 V was a moderate value considering the band gap energies⁴⁰. Thus it is noteworthy that a photovoltage increment of ~0.1 V and the enhanced fill factor obtained using CdS played a critical role in driving the overall water splitting.

Photon utilisation capability of the BiVO₄-Sb₂Se₃ tandem cell was confirmed by IPCE measurements. For BiVO₄, photons up to ~510 nm (*E*_g of 2.45 eV) could be converted and the absorption current density, which represents the maximum photocurrent density under the absorbance of BiVO₄, was calculated to be 5.5 mA cm⁻² (Supplementary Fig. 14b). Sum of the photon flux before and after passing through BiVO₄ up to the wavelength of 1033 nm (~1.2 eV, *E*_g of Sb₂Se₃) was calculated to be 39.9 and 24.4 mA cm⁻², respectively, which are much higher than the photocurrent of BiVO₄ at the top of the tandem cell configuration.

We compared BiVO₄ and Sb₂Se₃ in two different bias conditions: high bias near short circuit of the individual photoelectrode (1.0 V_{RHE} for photoanode and 0.1 V_{RHE} for photocathode; Supplementary Fig. 19) and operating bias at ‘actual’ operating point (0.4 V_{RHE} for both the photocathode and photoanode; Fig. 5d). In both cases, a broad range of photons could be effectively utilised by the synergetic effect of BiVO₄ (to 510 nm) and Sb₂Se₃ (from 450 to 1000 nm). In case of the high bias condition, both the photocathode and photoanode showed a quite high IPCE (~70% at 450 nm for BiVO₄ and ~60%

for Sb₂Se₃). The photocurrent calculated from the IPCE was 3.2 mA cm⁻² for the BiVO₄ photoanode. In addition, the photocurrent of the Sb₂Se₃ photocathodes was 18.5 and 10.3 mA cm⁻² with or without BiVO₄, respectively. These values are in a good agreement with photocurrents shown in the *J*-*V* curves (Supplementary Fig. 18). On the other hand, as expected, a lower IPCE was observed under the operating bias (0.4 V_{RHE}): ~25% at 450 nm for BiVO₄ and ~15% for Sb₂Se₃, as shown in Fig. 5d. The photocurrent density calculated using the IPCE spectra of BiVO₄ at 0.4 V_{RHE} was about 1.1 mA cm⁻², which is similar to the values shown by the *J*-*V* curve (Supplementary Fig. 18). However, the photocurrent density of Sb₂Se₃ photocathodes at 0.4 V_{RHE} with and without BiVO₄ were 5.0 and 2.2 mA cm⁻², respectively, which are higher than the photocurrents shown by the *J*-*V* curve. This discrepancy between the photocurrent density at 0.4 V_{RHE} demonstrated by the IPCE and *J*-*V* curve can be attributed to the light-intensity-dependent carrier mobility of Sb₂Se₃. As the carrier mobility of Sb₂Se₃ is much higher under low-intensity light³², Sb₂Se₃ photocathodes showed a better fill factor in IPCE measurement conditions (~100 μW cm⁻²) compared with the 1 sun conditions (100 mW cm⁻²), thereby resulting in a higher photocurrent according to the IPCE spectra at 0.4 V_{RHE}. The D4 tandem cell consisting of Sb₂Se₃ and BiVO₄ operated stably for over 10 h without any noticeable degradation in the photocurrent density (Fig. 5e). The efficiency and stability of our Sb₂Se₃-based tandem cells are comparable to those of the best-performing tandem cells containing other types of photocathode materials (vide infra). Finally, a larger tandem cell was constructed using a BiVO₄ photoanode (0.81 cm⁻²) and a Sb₂Se₃ photocathode (0.35 cm⁻²)

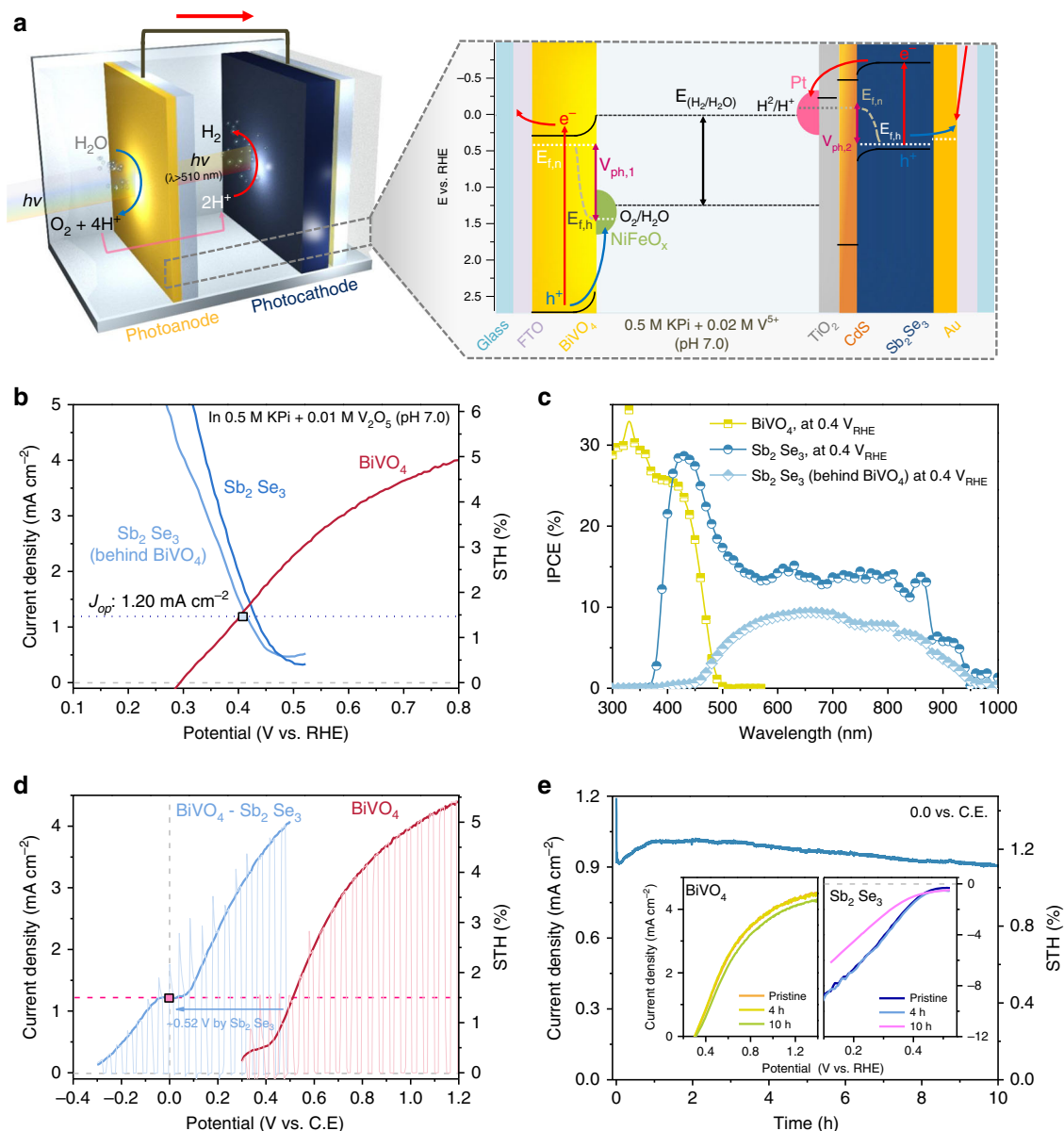


Fig. 5 Sb₂Se₃ photocathode-BiVO₄ photoanode for solar overall water splitting PEC cell. **a** Scheme of the NiFeO_x/H₂Mo:BiVO₄/FTO-Pt/TiO₂/CdS/Sb₂Se₃/Au/FTO tandem cell operating in pH 7.0 phosphate buffer. **b** J-V curve for the photoanode and photocathode; the operating point is marked for the tandem cell (photoelectrode active area: 0.32 cm²). **c** Two-electrode measurements for photoanode-counter electrode (C.E.) and photoanode-photocathode tandem cells (active area: 0.28 cm²). **d** IPCE at 0.4 V_{RHE} measured for the photoanode and photocathodes. **e** Photocurrent generation under short circuit conditions (O against counter electrode) of the photoanode-photocathode tandem cell. All analyses were conducted in 0.5 M phosphate buffer + 0.01 M V₂O₅ (pH 7.0) at a scan rate of 20 mV s⁻¹. Distance between the photoanode and photocathode was $\sim 0.5 \text{ cm}$. Source data used to generate this figure can be found in the Source Data file.

under simulated ~ 3 sun, which clearly demonstrated a constant generation of O₂ and H₂ gas evolution (Supplementary video 1, Supplementary Fig. 20).

Discussion

Even though we report herein the first demonstration of unbiased water splitting using a Sb₂Se₃ photocathode in a single reactor, better tandem cell systems are likely achievable by using two different electrolytes that are separately optimised for each photoelectrode (e.g. pH 1 for Sb₂Se₃ and pH 9 borate for BiVO₄) along with a bipolar membrane⁴¹ or stabilising both the photocathode and photoanode using additives (e.g. chelating agent to deter poisoning) in the electrolyte⁴². Bearing in mind its short history

and potential for further enhancement, the performance of the Sb₂Se₃-based tandem cell (STH efficiency of 1.5% and stability of over 10 h) is quite remarkable particularly in comparison with previously reported results for photocathode-photoanode tandem cells⁴ (Fig. 6a, Table 1 in Supplementary Information). We categorised the tandem cells based on the bottom light absorbers (silicone based, III-V, Cu-chalcogenides, metal oxides, and perovskites). Most of them used BiVO₄, which is currently the most suitable photoanode material and ensures good transparency ($\sim 80\%$ beyond photon utilisation threshold ($\sim 520 \text{ nm}$))¹⁰. It was found that the efficiency of the BiVO₄-Sb₂Se₃ tandem cell (1.5% STH) was not the highest when compared to that of BiVO₄-CIGS (3.7%)⁴³, BiVO₄-Cu₂O (3.0%)⁴⁴, and BiVO₄-c-Si (2.1%)⁴¹. Considering the cost of materials (much lower than that of CIGS),

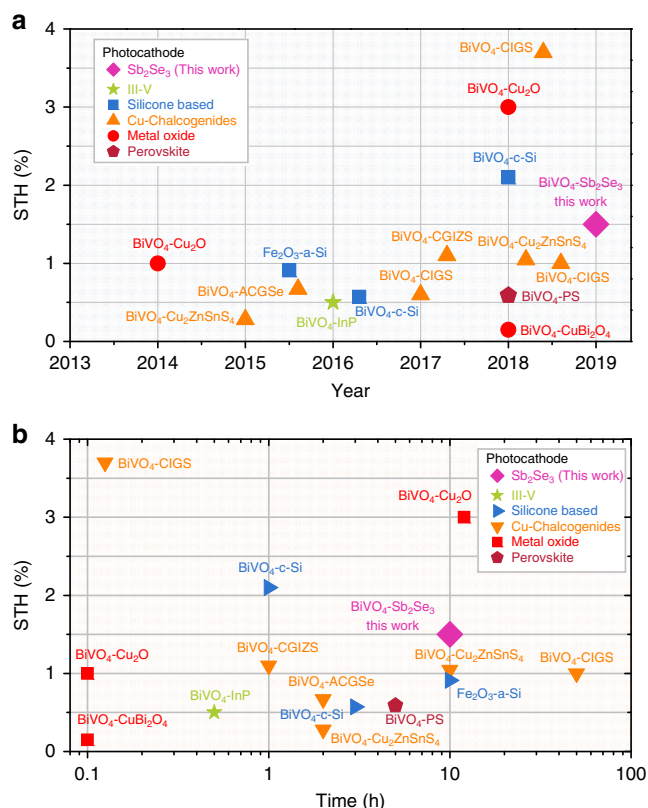


Fig. 6 Efficiency and stability benchmarks for photoanode-photocathode D4 tandem cell. **a** Solar-to-hydrogen efficiencies reported in recent years and **b** their operation duration. All reports are summarised in Supplementary Table 1.

small band gap (compared to that of Cu₂O, $E_g \sim 2.0$ eV), simple preparation, and low material usage (compared to that of Czochralski-grown Si wafer and complicated Si microwires), the >1% STH can be considered a significant milestone for PEC tandem cells. Moreover, 10 h of stability is also the best result reported for photoanode-photocathode tandem cells except for the 20 h stability achieved by the expensive CIGS-based photocathodes⁴⁵ (Fig. 6b). The exceptional performance and stability of the Sb₂Se₃ photocathode presented here, as well as several desirable material characteristics of Sb₂Se₃ such as its high α , optimal band gap of ~ 1.2 eV, and comparable photovoltage to that of c-Si (~ 0.5 V), clearly present a promising pathway towards realising a competitive overall water splitting PEC cell system, which could potentially result in an STH of approximately 10% using BiVO₄ photoanodes whose E_g is 2.4 eV (Supplementary Fig. 21a). In order to demonstrate a higher STH efficiency, the areas of focus should include enhancing both the photovoltage and fill factor through interface engineering, such as the recently reported dipole engineering at the buried junction⁴⁶. In addition, the development of an ideal photoanode material with an E_g close to 1.8 eV could potentially enable an STH efficiency of >20% on using the Sb₂Se₃ photocathode (Supplementary Fig. 21b). Although the value of STH 1.5% is not superior in comparison to that of other systems, such as photovoltaic-electrolytic systems (average 10–20%), buried-junction photoelectrodes (10–15%), and photovoltaic-PEC systems (3–8%), because of the simplicity of the photoanode-photocathode system, the price of hydrogen produced from such a system will be lower. Therefore, not only the STH efficiency but also the cost should be considered when comparing such systems. The reported STH efficiencies of the photoanode-photocathode

tandem system are increasing very rapidly (Fig. 6), which suggests increasing research interest in reducing the complexity of overall water splitting devices⁴.

In summary, we have demonstrated a high-performance photocathode using a low-cost Sb₂Se₃ semiconductor, which has a small E_g (~ 1.2 eV), good optoelectronic properties, and no secondary phase. By suppressing the growth kinetics during the CSS deposition, a compact and pinhole-free Sb₂Se₃ thin film was obtained, which enabled a highest photocurrent density of up to 30 mA cm⁻² by avoiding recombination and accelerating charge separation through well-aligned (Sb₄Se₆)_n ribbons. Inserting a CdS layer between Sb₂Se₃ and TiO₂ increased the onset potential and consequently improved the HC-STH efficiency up to 3.4%. Finally, by combining the material with a BiVO₄ photoanode, unbiased overall water splitting was achieved with impressive efficiency ($\sim 1.5\%$) and high stability of 10 h. These performances and stability significantly surpass those of previously reported Sb₂Se₃ photocathodes and are comparable to those of other expensive thin film photocathodes. Given the relatively short history of photoelectric materials, it is expected that rapid progress of Sb₂Se₃ photocathodes will lead to better efficiency in the near future and our findings represent an important demonstration of a photocathode-photoanode-based PEC device. We believe that the emerging Sb₂Se₃ substrate can be an attractive breakthrough material for practical solar fuel production.

Methods

Preparation of Sb₂Se₃ thin films. Sb₂Se₃ films were deposited via a two-step CSS process³¹ using a custom-made CSS system. First, a compact layer was grown from stoichiometric Sb₂Se₃ (Alfa Aesar, 99.999% metals basis) using a source temperature of 340 °C and a substrate temperature of 390 °C for 2 min at a pressure of 0.05 mbar. Subsequently, deposition was completed using a source temperature of 460 °C for 15 min and a pressure of 13 mbar. These films were then cooled either slowly or fast, by turning the heater off and flowing N₂ over the sample at a rate of either 0 or 5 L min⁻¹, respectively.

Deposition of overlayers and catalysts for photocathodes. CdS layers were deposited by the chemical bath deposition (CBD) method. Prior to CBD, the sample was pre-treated in a bath containing a solution of CdSO₄ (Sigma Aldrich, 99.99%) and NH₄OH (Duksan, 28 wt%) at 60 °C for 10 min. CBD of CdS was performed by immersing the pre-treated sample in a solution containing CdSO₄, thiourea (99%, Sigma Aldrich), deionised (DE) water, and NH₄OH for 5 min at 60 °C. TiO₂ layers were deposited using an ALD system (Lucida D100, NCD Inc.). The ALD process was performed at 150 °C, with tetrakis(dimethylamido)titanium (TDMAT) and H₂O as the Ti and O sources, respectively. A total of 600 ALD cycles were carried out, each of which comprised a TDMAT pulse of 0.3 s followed by 15 s of N₂ purging and a H₂O pulse of 0.2 s followed by 15 s of N₂ purging. The approximate growth rate of TiO₂ was 0.55 Å per cycle, as estimated using an ellipsometer. The Pt catalyst was sputtered onto the TiO₂-coated Sb₂Se₃ electrode using an Auto Sputter Coater (Ted Pella, Redding, CA, USA) under an applied current of 10 mA for 120 s. A galvanostatic photo-deposition technique was used for RuO_x deposition. The prepared photoelectrodes were immersed in a 1.3 mM solution of KRuO₄ at a current density of $-28.3 \mu\text{A cm}^{-2}$ for 15 min under simulated 1 sun illumination.

Preparation of BiVO₄ films. All chemicals used in this study were of analytical grade and used without further purification. BiVO₄ film was prepared by a modified metal-organic decomposition method according to our previously reported procedure⁴⁷ with slight modifications. In brief, 291 mg of Bi(NO₃)₃·5H₂O (99.8%; Kanto Chemicals) and 163 mg of VO(acac)₃ (98.0%; Sigma Aldrich) were dissolved in 15 mL of acetyl acetone (>99.0%; Kanto Chemicals). As the dopant solution, 0.03 M MoO₂(acac)₂ (98.0%; Sigma Aldrich) in acetyl acetone (>99.0%; Kanto Chemicals) was prepared. A 0.2 M Bi(NO₃)₃·5H₂O (99.8%; Kanto Chemicals) solution dissolved in acetic acid (>99.0%; Kanto Chemicals) was used to compensate the Mo precursor-added solution. For Mo doping, a Bi:(V+Mo) = 1:1 atomic ratio was used for preparing the 1% Mo:BiVO₄ films. To fabricate the BiVO₄ film, 35 μL of the solution was dropped on a FTO glass sample (2 cm \times 2.5 cm) and dried for 10 min in Ar atmosphere. The FTO glass (TEC 8; Pilkington) was cleaned using ethanol + 35 wt% H₂O₂ (Samchun Chemical) used in a ratio of 5:1 under sonication (~ 20 min) and washed with copious amounts of ethanol and finally stored in 2-propanol before use. The greenish transparent precursor film was calcined at 550 °C for 30 min to form a yellow BiVO₄ film. After the annealing process, the 2 cm \times 2.5 cm BiVO₄/FTO was split to obtain photoanodes with a net

irradiation area of 0.36 cm^2 connected by silver paste and copper wire and sealed with epoxy resin.

Hydrogen treatment of metal oxide films. Hydrogen treatment was conducted using the borohydride decomposition method reported by Hao et al.⁴⁸. First, 16 mmol of NaBH_4 (>98%; Sigma Aldrich) was introduced in a 200-mL alumina crucible and another smaller alumina bottle (15 mL) was introduced to the NaBH_4 powder. In this smaller bottle, an as-prepared metal oxide film ($2\text{ cm} \times 2.5\text{ cm}$) was placed and finally the 200-mL alumina crucible was covered with an alumina cover. This reactor was placed in an already heated furnace at 500°C for 30 min. Then the crucible was taken out from the furnace and cooled naturally.

NiFeO_x co-catalyst deposition on BiVO₄ film. The NiFeO_x co-catalysts were deposited by photo-assisted electrodeposition under air mass (AM) 1.5 G illumination according to a reported procedure⁴⁹. In all, 60 mg of $\text{Fe}(\text{SO}_4)_2 \cdot 7\text{H}_2\text{O}$ (>99%; Sigma Aldrich) and 20 mg of $\text{Ni}(\text{SO}_4)_2 \cdot 6\text{H}_2\text{O}$ (99%; Sigma Aldrich) were put in a glass bottle and 200 mL of 0.5 M KHCO_3 (pH 8.3, purged with Ar gas for 30 min before use) was introduced, resulting in a transparent and yellow solution. For deposition, under illumination (AM 1.5 G, 100 mW cm^{-2}), linear sweep voltammetry was conducted with a bias of -0.3 to 0.5 V against the reference electrode (Ag/AgCl) for 12–15 times with pre-treatment of -0.3 V for 5 s. Sequential linear sweep voltammetry resulted in reduced current density and over-deposition of NiFeO_x . After deposition, the photoelectrode was taken out and washed with copious amounts of DI water. Right after being taken out, the photoelectrode showed a slightly darkened colour ($\text{Ni}(\text{OH})_2$ species) but gradually changes to a colour identical to that of the photoelectrode before NiFeO_x deposition. The photoelectrodes were stored in an Ar gas-filled bottle before use.

Characterisation. The surface morphology of Sb_2Se_3 thin films were analysed via field-emission scanning electron microscope (JSM-7001F, JEOL Ltd, Tokyo, Japan). The crystallinity of the samples was investigated using XRD (MiniFlex 600, Rigaku, Tokyo, Japan) with Cu K α radiation ($\lambda = 1.54178\text{ \AA}$). The surface reflectance of the Sb_2Se_3 thin films was measured using an ultraviolet–visible (UV–vis) spectrophotometer (V-670, JASCO, Easton, MD, USA). UV–Vis absorbance of BiVO_4 was recorded with a UV/Vis spectrometer (UV-2401PC, Shimadzu). As a reference, BaSO_4 powder was used. In addition, KPFM (SPA 400, Seiko Instrument Inc., Chiba, Japan) measurements were performed using a gold-coated cantilever (SI-DF3-A).

Determination of PEC performance. PEC measurements for Sb_2Se_3 photocathodes were performed in a typical three-electrode system with a Ag/AgCl/KCl (4 M) reference electrode and a Pt wire counter electrode. The Sb_2Se_3 photocathodes were submerged in an acidic (H_2SO_4 , pH ~ 1) or a neutral (phosphate buffer, pH ~ 6.25) electrolyte and simulated solar light illumination. Calibration of the 1-sun level was performed using a standard Si reference cell certified by the Newport Corporation, consisting of a readout device and a $2 \times 2\text{ cm}^2$ calibrated solar cell made of monocrystalline silicon. During calibration, the Si reference cell was located at the same position of the sample for PEC measurement. The scan rate for the J – V curves was 5 mV s^{-1} . For Sb_2Se_3 photocathodes, the applied potentials were recorded against the RHE to allow comparison with previously reported results, employing the relationship $E_{\text{RHE}} = E_{\text{Ag/AgCl}} + 0.059\text{ pH} + 0.197$. IPCE for Sb_2Se_3 photocathodes was measured with an electrochemical workstation (Zennium, Zahner, Germany) combined with a potentiostat (PP211, Zahner, Germany) under monochromatic light.

PEC performance of the BiVO_4 photoanode was measured with a photoanode as the working electrode, Pt mesh as the counter electrode, and Ag/AgCl (3 M NaCl) as the reference electrode. The scan rate for the J – V curves was 20 mV s^{-1} . For electrolyte, 0.5 M potassium phosphate (K_2HPO_4 or KPi) buffer + 0.01 M V_2O_5 (pH 7.0) was used as a standard electrolyte as reported previously for the borate buffer (pH 9.5). To accelerate dissolution of V_2O_5 , it was placed in oven at 80°C for 3 h. The pH of the KPi buffer barely changed (<0.01) while the pH of 8 or 9 showed a noticeable change that could be compensated by adding a small amount of 0.5 M KOH. Potentials were recorded with correction according to the Nernst relationship $E_{\text{RHE}} = E_{\text{Ag/AgCl}} + 0.0591\text{ pH} + 0.209$, in which $E_{\text{Ag/AgCl}}$ is the applied bias potential and 0.209 is a conversion factor from the Ag/AgCl electrode to the RHE scale. The electrochemical data for BiVO_4 photoanodes were recorded by using a potentiostat (IviumStat, Ivium Technologies). A 300 W Xenon lamp was used to produce simulated 1 sun light irradiation conditions (AM 1.5 G, 100 mW cm^{-2}) employing a solar simulator (Oriol 91160) with an AM 1.5 G filter calibrated with a reference cell certified by the National Renewable Energy Laboratories, USA.

For the BiVO_4 – Sb_2Se_3 tandem cell, black masked (0.32 – 0.36 cm^2) photoelectrodes were aligned with a spacing of $\sim 0.5\text{ cm}$ in a single electrolyte bed reactor. Photocurrent of Sb_2Se_3 was recorded with or without the BiVO_4 photoelectrode (fully modified, $\text{NiFeO}_x/\text{H}_2\text{Mo:BiVO}_4$) under backward scan (-0.5 – 0 V_{RHE}). The BiVO_4 photoelectrode was scanned in the forward scan (0.2 – $1.4\text{ V}_{\text{RHE}}$). For the BiVO_4 – Sb_2Se_3 two-electrode full cell, BiVO_4 was set as the working electrode and Sb_2Se_3 was set as the counter electrode. Bias was applied towards the counter electrode and thus 0 V against the counter electrode indicated a 0 V potential applied to the full cell. For linear sweep, forward scan was applied for

the BiVO_4 –Pt rod (0.3 – 1.3 V) or BiVO_4 – Sb_2Se_3 (-0.3 to 0.5 V). All scans were performed with 10 s of pre-treatment at the initial potential at a speed of 20 mV s^{-1} .

IPCE measurements for BiVO_4 and Sb_2Se_3 behind BiVO_4 were conducted using a 300 W Xe lamp as the light source with a liquid infrared filter and a monochromator (Oriol Cornerstone 130 1/8 m monochromator) with a bandwidth limit of 5 nm . The intensity of light was measured before IPCE measurements by a photodiode detector (Oriol 70260). Calculation of IPCE was carried out according to the equation:

$$\text{IPCE}(\%) = \frac{1240 \times J}{\lambda \times P} \times 100 \quad (1)$$

where J = photocurrent density (mA cm^{-2}), P = light power density (mW cm^{-2}) at λ , and λ = wavelength of incident light (nm). J was gathered under the condition that the PEC cell individually installed and the constant potential applied for a photoelectrode and wavelength of illuminated beam ($1\text{ cm} \times 1\text{ cm}$) was periodically changed. The active area of the characterised photoelectrode was preferably smaller than this beam source (0.32 – 0.36 cm^2). The scanning wavelength range was 300 – 1100 nm with an interval of 10 nm/7 s .

Data availability

The data that support the plots within this paper and other findings of this study are available from the corresponding author upon reasonable request. The source data underlying Figs. 2, 3e, f, 4b–d, 5b–e, and 6 and Supplementary Figs. 2, 3, 4, 5c, 7, 8, 9, 10, 11a, 13, 14, 15, 16, 17, 18b–d, 19, and 21a are provided as a Source Data file.

Received: 2 August 2019; Accepted: 24 January 2020;

Published online: 13 February 2020

References

- Cheng, W.-H. et al. Monolithic photoelectrochemical device for direct water splitting with 19% efficiency. *ACS Energy Lett.* **3**, 1795–1800 (2018).
- Turner, J. A. Shining a light on solar water splitting—response. *Science* **344**, 469–470 (2014).
- Sivula, K. & Van De Krol, R. Semiconducting materials for photoelectrochemical energy conversion. *Nat. Rev. Mater.* **1**, 15010 (2016).
- Kim, J. H., Hansora, D., Sharma, P., Jang, J.-W. & Lee, J. S. Toward practical solar hydrogen production—an artificial photosynthetic leaf-to-farm challenge. *Chem. Soc. Rev.* **48**, 1908–1971 (2019).
- Yao, T., An, X., Han, H., Chen, J. Q. & Li, C. Photoelectrocatalytic materials for solar water splitting. *Adv. Energy Mater.* **8**, 1800210 (2018).
- Hu, S., Xiang, C., Haussener, S., Berger, A. D. & Lewis, N. S. An analysis of the optimal band gaps of light absorbers in integrated tandem photoelectrochemical water-splitting systems. *Energy Environ. Sci.* **6**, 2984–2993 (2013).
- Pinaud, B. A. et al. Technical and economic feasibility of centralized facilities for solar hydrogen production via photocatalysis and photoelectrochemistry. *Energy Environ. Sci.* **6**, 1983–2002 (2013).
- Fujishima, A. & Honda, K. Electrochemical photolysis of water at a semiconductor electrode. *Nature* **238**, 37–38 (1972).
- Tamirat, A. G., Rick, J., Dubale, A. A., Su, W.-N. & Hwang, B.-J. Using hematite for photoelectrochemical water splitting: a review of current progress and challenges. *Nanoscale Horiz.* **1**, 243–267 (2016).
- Kim, J. H. & Lee, J. S. Elaborately modified BiVO_4 photoanodes for solar water splitting. *Adv. Mater.* **31**, 1806938 (2019).
- Paracchino, A., Laporte, V., Sivula, K., Grätzel, M. & Thimsen, E. Highly active oxide photocathode for photoelectrochemical water reduction. *Nat. Mater.* **10**, 456 (2011).
- Yang, W. et al. Molecular chemistry-controlled hybrid ink-derived efficient $\text{Cu}_2\text{ZnSnS}_4$ photocathodes for photoelectrochemical water splitting. *ACS Energy Lett.* **1**, 1127–1136 (2016).
- Yu, Y.-X. et al. Solution-processed Cu_2S photocathodes for photoelectrochemical water splitting. *ACS Energy Lett.* **3**, 760–766 (2018).
- Oh, Y., Yang, W., Kim, J., Jeong, S. & Moon, J. Enhanced photocurrent of transparent CuFeO_2 photocathodes by self-light-harvesting architecture. *ACS Appl. Mater. Interfaces* **9**, 14078–14087 (2017).
- Song, A. et al. Cu:NiO as a hole-selective back contact to improve the photoelectrochemical performance of CuBi_2O_4 thin film photocathodes. *J. Mater. Chem. A* **7**, 9183–9194 (2019).
- Zhang, L. et al. Solution-processed CuSbS_2 thin film: a promising earth-abundant photocathode for efficient visible-light-driven hydrogen evolution. *Nano Energy* **28**, 135–142 (2016).
- Huang, X. et al. Simple eco-friendly synthesis of the surfactant free SnS nanocrystal toward the photoelectrochemical cell application. *Sci. Rep.* **7**, 16531 (2017).
- Yang, W. & Moon, J. Rapid advances in antimony triselenide photocathodes for solar hydrogen generation. *J. Mater. Chem. A* **7**, 20467 (2019).

19. Wang, L. et al. Stable 6%-efficient Sb_2Se_3 solar cells with a ZnO buffer layer. *Nat. Energy* **2**, 17046 (2017).
20. Chen, C. et al. Characterization of basic physical properties of Sb_2Se_3 and its relevance for photovoltaics. *Front. Optoelectron.* **10**, 18–30 (2017).
21. Ghosh, G. The Sb–Se (antimony–selenium) system. *J. Phase Equilibria* **14**, 753–763 (1993).
22. Prabhakar, R. R. et al. Photocorrosion-resistant Sb_2Se_3 photocathodes with earth abundant MoSx hydrogen evolution catalyst. *J. Mater. Chem. A* **5**, 23139–23145 (2017).
23. Kim, J. et al. Self-oriented Sb_2Se_3 nanoneedle photocathodes for water splitting obtained by a simple spin-coating method. *J. Mater. Chem. A* **5**, 2180–2187 (2017).
24. Yang, W. et al. Adjusting the anisotropy of 1D Sb_2Se_3 nanostructures for highly efficient photoelectrochemical water splitting. *Adv. Energy Mater.* **8**, 1702888 (2018).
25. Tan, J. et al. Fullerene as a photoelectron transfer promoter enabling stable TiO_2 -protected Sb_2Se_3 photocathodes for photo-electrochemical water splitting. *Adv. Energy Mater.* **9**, 1900179 (2019).
26. Lee, H. et al. Cu-doped NiOx as effective hole-selective layer for high-performance Sb_2Se_3 photocathode for photoelectrochemical water splitting. *ACS Energy Lett.* **4**, 995–1003 (2019).
27. Park, J. et al. Efficient solar to hydrogen conversion from neutral electrolytes using morphology-controlled Sb_2Se_3 light absorber. *ACS Energy Lett.* **4**, 517–526 (2019).
28. Phillips, L. J. et al. Current enhancement via a TiO_2 window layer for $\text{CSS Sb}_2\text{Se}_3$ solar cells: performance limits and high Voc. *IEEE J. Photovolt.* **9**, 544–551 (2019).
29. Major, J. D. et al. A low-cost non-toxic post-growth activation step for CdTe solar cells. *Nature* **511**, 334–337 (2014).
30. Guo, Q. et al. The growth of a $\text{CH}_3\text{NH}_3\text{PbI}_3$ thin film using simplified close space sublimation for efficient and large dimensional perovskite solar cells. *Energy Environ. Sci.* **9**, 1486–1494 (2016).
31. Hutter, O. S., Phillips, L. J., Durose, K. & Major, J. D. 6.6% efficient antimony selenide solar cells using grain structure control and an organic contact layer. *Sol. Energy Mater. Sol. Cells* **188**, 177–181 (2018).
32. Yang, W. et al. Time-resolved observations of photo-generated charge-carrier dynamics in Sb_2Se_3 photocathodes for photoelectrochemical water splitting. *ACS Nano* **12**, 11088–11097 (2018).
33. Zhang, J. et al. Alternative back contacts for Sb_2Se_3 solar cells. *Sol. Energy* **182**, 96–101 (2019).
34. Tilley, S. D., Schreier, M., Azevedo, J., Stefik, M. & Graetzel, M. Ruthenium oxide hydrogen evolution catalysis on composite cuprous oxide water-splitting photocathodes. *Adv. Funct. Mater.* **24**, 303–311 (2014).
35. Chen, C. et al. Efficiency improvement of Sb_2Se_3 solar cells via grain boundary inversion. *ACS Energy Lett.* **3**, 2335–2341 (2018).
36. Vishwakarma, M. et al. A direct measurement of higher photovoltage at grain boundaries in CdS/CZTSe solar cells using KPFM technique. *Sol. Energy Mater. Sol. Cells* **183**, 43–40 (2018).
37. Kim, G. Y. et al. Nanoscale investigation of surface potential distribution of $\text{Cu}_2\text{ZnSn}(\text{S},\text{Se})_4$ thin films grown with additional NaF layers. *Nano Convergence* **1**, 27 (2014).
38. Luo, J. et al. Cu_2O nanowire photocathodes for efficient and durable solar water splitting. *Nano Lett.* **16**, 1848–1857 (2016).
39. Prévot, M. S. & Sivula, K. Photoelectrochemical tandem cells for solar water splitting. *J. Phys. Chem. C* **117**, 17879–17893 (2013).
40. Mayer, M. T. Photovoltage at semiconductor–electrolyte junctions. *Curr. Opin. Electrochem.* **2**, 104–110 (2017).
41. Visselaar, W. et al. Spatial decoupling of light absorption and catalytic activity of Ni–Mo-loaded high-aspect-ratio silicon microwire photocathodes. *Nat. Energy* **3**, 185 (2018).
42. Kaneko, H., Minegishi, T., Kobayashi, H., Kuang, Y. & Domen, K. Suppression of poisoning of photocathode catalysts in photoelectrochemical cells for highly stable sunlight-driven overall water splitting. *J. Chem. Phys.* **150**, 041713 (2019).
43. Kobayashi, H. et al. Development of highly efficient $\text{CuIn}_{0.5}\text{Ga}_{0.5}\text{Se}_2$ -based photocathode and application to overall solar driven water splitting. *Energy Environ. Sci.* **11**, 3003–3009 (2018).
44. Pan, L. et al. Boosting the performance of Cu_2O photocathodes for unassisted solar water splitting devices. *Nat. Catalysis* **1**, 412 (2018).
45. Higashi, T. et al. Overall water splitting by photoelectrochemical cells consisting of $(\text{ZnSe})_{0.85}(\text{CuIn}_{0.7}\text{Ga}_{0.3}\text{Se}_2)_{0.15}$ photocathodes and BiVO_4 photoanodes. *Chem. Commun.* **53**, 11674–11677 (2017).
46. Wick-Jaliat, R. et al. Stable and tunable phosphonic acid dipole layer for band edge engineering of photoelectrochemical and photovoltaic heterojunction devices. *Energy Environ. Sci.* **12**, 1901–1909 (2019).
47. Kim, J. H. et al. Wireless solar water splitting device with robust cobalt-catalyzed, dual-doped BiVO_4 photoanode and perovskite solar cell in tandem: a dual absorber artificial leaf. *ACS Nano* **9**, 11820–11829 (2015).
48. Hao, Y., Deng, J., Zhou, L., Sun, X. & Zhong, J. Depth-reduction induced low onset potential of hematite photoanodes for solar water oxidation. *RSC Adv.* **5**, 31086–31090 (2015).
49. Li, F. et al. An iron-based thin film as a highly efficient catalyst for electrochemical water oxidation in a carbonate electrolyte. *Chem. Commun.* **52**, 5753–5756 (2016).

Acknowledgements

This work was supported by a National Research Foundation (NRF) of Korea grant (No. 2012R1A3A2026417); a Creative Materials Discovery Program (NRF-2018M3D1A1058793) funded by the Ministry of Science and ICT; the Korea Center for Artificial Photosynthesis (KCAP, No. 2009–0093880), funded by the MSIT; Project No. 10050509 funded by the MOTIE of Republic of Korea; and the UK EPSRC project number EP/N014057/1.

Author contributions

W.Y. conceived the idea, organised the collaboration, conducted experiments, analysed the data, and wrote the manuscript. J.H.K. prepared the BiVO_4 photoanodes, tested the tandem device, and co-wrote the manuscript. O.S.H. and L.J.P. prepared and optimised the Sb_2Se_3 thin films via the CSS method. J.T., J.P. and H.L. assisted in device optimisation and data analysis for the Sb_2Se_3 photocathodes. J.D.M. helped to the idea and manuscript preparation. J.S.L. directed the research and contributed to the writing of the manuscript. J.M. designed and supervised the project, directed the research, and contributed to the writing of the manuscript.

Competing interests

The authors declare no competing interests.

Additional information

Supplementary information is available for this paper at <https://doi.org/10.1038/s41467-020-14704-3>.

Correspondence and requests for materials should be addressed to J.D.M., J.S.L. or J.M.

Peer review information *Nature Communications* thanks the anonymous reviewers for their contributions to the peer review of this work. Peer review reports are available.

Reprints and permission information is available at <http://www.nature.com/reprints>

Publisher's note Springer Nature remains neutral with regard to jurisdictional claims in published maps and institutional affiliations.



Open Access This article is licensed under a Creative Commons Attribution 4.0 International License, which permits use, sharing, adaptation, distribution and reproduction in any medium or format, as long as you give appropriate credit to the original author(s) and the source, provide a link to the Creative Commons license, and indicate if changes were made. The images or other third party material in this article are included in the article's Creative Commons license, unless indicated otherwise in a credit line to the material. If material is not included in the article's Creative Commons license and your intended use is not permitted by statutory regulation or exceeds the permitted use, you will need to obtain permission directly from the copyright holder. To view a copy of this license, visit <http://creativecommons.org/licenses/by/4.0/>.

© The Author(s) 2020